Monte Carlo simulation of x-ray absorption and electron drift in gaseous xenon

T. H. V. T. Dias and F. P. Santos
Departamento de Física, Universidade de Coimbra, 3000 Coimbra, Portugal

A. D. Stauffer
Physics Department, York University, Toronto, Canada M3J 1P3

C. A. N. Conde
Departamento de Física, Universidade de Coimbra, 3000 Coimbra, Portugal
(Received 1 June 1993)

A detailed Monte Carlo simulation model has been developed to study the absorption of soft x rays and the subsequent behavior of the resulting electrons under the influence of an applied electric field in gaseous xenon. All relevant physical processes are included from the initial photoionization through the subsequent decay of the residual ion to the scattering and drift of the electrons resulting from the interactions with the background gas. Details are provided for the cross sections and decay rates employed as well as the criteria used to terminate the simulation, depending on the information or results required. Examples of its use in modeling gaseous radiation detectors are included.

PACS number(s): 32.80.−t, 29.40.Mc, 29.40.Cs, 34.90.+q

I. INTRODUCTION

Gaseous detectors for x rays [1] are commonly used in material analysis by x-ray fluorescence techniques, x-ray diffractometers, plasma physic studies, etc., as well as in x-ray astronomy, high-energy physics, and medical instrumentation. In order to fully understand the characteristics of such detectors, a comprehensive study of their behavior is required. Although the physics involved in such detectors has been studied using Boltzmann analysis [2–4], this method is not capable of fully investigating the detailed processes occurring in the detectors. These involve for a start the photoionization of the gas atoms by the x-ray photons, followed by the emission of cascade electrons by the atoms via Auger–Coster-Kronig decays and shake-off ionization together with the emission and reabsorption of fluorescence photons. The creation of these first electrons requires a detailed description of the atomic processes involved. Within the drift zone of the detector, these electrons produce further electrons by ionizing gas atoms until their energy drops below the ionization threshold, i.e., until the so-called primary-electron cloud is fully developed. Further along, these primary electrons gain energy from an applied electric field and may produce additional photons (the secondary scintillation) or second electrons as a result of inelastic collisions with the gaseous atoms in the detector. To a first approximation, the number of primary electrons produced is proportional to the x-ray energy, and the number of secondary scintillation photons or secondary electrons is proportional to the number of primary electrons. Hence either the secondary photons or the secondary electrons can provide information about the energy of the original x ray. Proportional counters measure the number of secondary electrons produced, while proportional scintillation counters measure the amount of vacuum ultraviolet (vuv) radiation emitted by the gas, normally at field strengths below that required to produce secondary electrons, i.e., avoiding charge multiplication. Xenon is often the gas of choice for these detectors because of its large x-ray-absorption cross section and scintillation efficiency. Detectors using xenon can be operated at room temperature and atmospheric pressure and usually employ a high-purity quartz window photomultiplier for the detection of the vuv scintillation. Other gases such as krypton or argon may also be used.

In this paper we describe a Monte Carlo simulation scheme that we have developed which takes into account all processes described above and subsequently follows individual electrons as they move through the gas under the influence of an applied electric field. Although we provide a detailed analysis for the case of xenon, our model can be extended easily to other monatomic gases provided the required atomic cross sections, decay rates, and electron-scattering cross sections are available.

Certain results using our simulation scheme have already been published elsewhere. We have carried out a careful study of the charge distribution of the residual xenon ions produced by x-ray absorption [5,6] and have investigated the size and shape of the primary electron cloud [7], the Fano factor F [8], the mean energy w to produce an electron-ion pair [9], and distortion effects in the soft-x-ray spectra due to the loss of primary electrons to the detector window [10,11]. Various electroluminescence parameters in gas proportional scintillation counters (GPSC) have also been analyzed [12,13]. Our initial attempt to simulate these detectors used a simplified unidimensional approach to study the reduced light output for reduced electric fields below the threshold for secondary-electron production [14]. All of these studies were carried out for xenon at atmospheric pressure and room temperature. Not only were we able to

reproduce the experimentally observed behavior but we could also explain the cause of such behavior and show that certain commonly held assumptions were incorrect. For example, for soft x rays, the parameter w as well as the Fano factor F are not independent of the photon energy, as commonly assumed, but have a nonlinear behavior with discrete jumps at the photoionization absorption edges.

In the next section we present the details of the x-ray-photon–xenon-atom interaction. In Sec. III the cross sections required to model the electron-atom collisions are presented. We describe our Monte Carlo simulation model in Sec. IV and provide some typical results in Sec. V.

II. X-RAY–ATOM INTERACTIONS IN XENON

A. Photoionization cross sections

When an x-ray is absorbed by a gaseous medium, it ionizes a gas atom. If the x ray has sufficient energy to photoionize an inner shell, this inner-shell vacancy is filled by an electron from the outer shells and, in the subsequent decay of the residual ion, the emission of further electrons or fluorescence photons will occur. Accurate knowledge of the atomic shell from which the photoelectron originates is thus required in order to determine the energy of the photoelectron as well as the decay paths of the ion and their relative probabilities.

Angle-integrated photoionization cross sections at fixed x-ray energies for the individual subshells $\sigma_{\rm ph}^{p}$ were taken, for energies lower than 4509 eV, from Kutzner, Radojevic, and Kelly [15], Band, Kharitonov, and Trzhaskovskaya [16], and Kennedy and Manson [17] for the M_1, $M_{2,3}$, $M_{4,5}$, N_1, $N_{2,3}$, $N_{4,5}$, O_1, and $O_{2,3}$ subshells. The sum of these partial cross sections agreed very well with the total cross section $\sigma_{\rm ph}^{T}$ given by West and Morton [18], Wuilleumier [19], and Saloman, Hubbell, and Scofield [20]. Since in the simulation we require these cross sections at arbitrary energies we used a linear interpolation of the cross section between the given energy values. We fitted the cross sections between the last two energy points in the form $aE_{\rm xr}^{-b}$, where $E_{\rm xr}$ is the x-ray energy, and used this form to extrapolate the cross sections to energies $E_{\rm xr}$ above 4509 eV. The binding energies (and hence the absorption edges) were obtained from Larkins [21]. Where we did not distinguish between individual subshells, we averaged the binding energies given there (for instance, we considered the M_2 and M_3 subshells as one).

Above the threshold for ionizing the L shell, the partial photoionization cross sections $\sigma_{\rm ph}^{p}$ for the L_1, L_2, and L_3 shells were obtained by subtracting the sum of the partial cross sections for the outer shells from the total cross sections. For this purpose, total cross-section values in this range were taken from Wuilleumier [19], and Saloman, Hubbell, and Scofield [20] and, at an energy just below the K shell ionization threshold, from Veigele [22]. Extrapolation of these cross sections was done using the analytic form given above with the values of exponent b being of the same order of magnitude. These various photoionization cross sections are shown in Fig. 1.

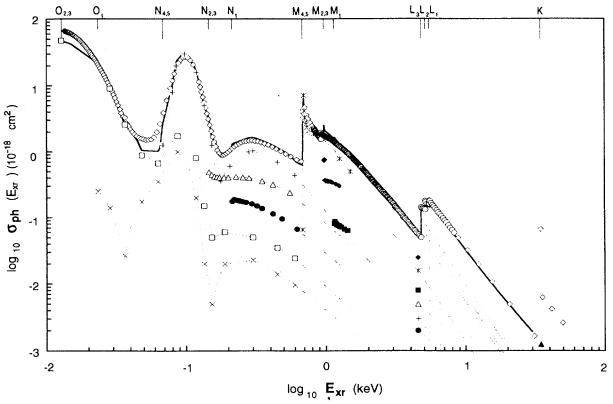

FIG. 1. Xenon photoionization cross sections $\sigma_{\rm ph}^{p}$ (partial) and $\sigma_{\rm ph}^{T}$ (total) vs x-ray energy $E_{\rm xr}$. $\sigma_{\rm ph}^{p}$: □,×,+ Kutzner, Radojevic, and Kelly [15] and Band, Kharitonov, and Trzhaskovskaya [16]; △,●,◆■,* Kennedy and Manson [17] and Band, Kharitorov, and Trzhaskovskaya [16]. $\sigma_{\rm ph}^{T}$: ◇ West and Morton [18], ○ Wuilleumier [19], and ▲ Veigele [22]. Continuous curves represent $\sigma_{\rm ph}^{p}$ (· · · ·) and $\sigma_{\rm ph}^{T}$ (——) photoionization cross sections adopted in this work.

Since we must also take into account the direction in which the photoelectron is emitted, we use the well-known angular differential cross section form for photoionization by unpolarized light

$$\frac{d\sigma_{\rm ph}^{p}}{d\Omega}=\frac{\sigma_{\rm ph}^{p}}{4\pi}[1-\tfrac{1}{2}\beta(\varepsilon)P_2(\cos\theta)] \tag{1}$$

for each subshell, where θ is the angle between the direction of the incident x ray and that of the emitted photoelectron, P_2 is the Legendre polynomial of degree 2, $\sigma_{\rm ph}^{p}$ is the partial photoionization cross section for subshell p, and the values of β for each subshell are given in [17]. Although the β asymmetry parameter exhibits a weak dependence on the photoelectron energy ε in the case of p and d subshells, we use their fixed high-energy value in all cases (i.e., we use $\beta=1$ for d subshells, $\beta=1.5$ for p subshells, and $\beta=2$ for s subshells).

B. Cascade decay rates

If, after photoionization, the residual ion is left in an excited state it will decay in general through a multistep cascade process [23,24] leading to a multiple charged ion in its lowest-energy state. Three distinct processes are involved in this decay.

Auger–Coster-Kronig transitions are radiationless transitions where an inner-shell vacancy is filled by an electron from an outer shell with a simultaneous emission of an electron from the same or some other outer shell. Thus the residual ion is left in a charge state one higher than before the transition and an additional electron is produced. The energy ε of the emitted electron is calculated by means of the $(z,z+1)$ approximation [25]

$$\varepsilon=\beta_{54}^{1}-\{\tfrac{1}{2}(B_{54}^{2}+B_{55}^{2})+\tfrac{1}{2}(B_{54}^{3}+B_{55}^{3})\} \tag{2}$$

where the superscript $i=1$ refers to the shell with the initial vacancy while $i=2,3$ refers to the shells with vacancies after the transition and B_z^i is the binding energy of the subshell i of the atom with nuclear charge z. The use of the average of the binding energies of one shell in xenon ($z=54$) with the corresponding shell in cesium ($z=55$) approximates the fact that the binding energy of a particular shell is greater in the ion than in the neutral atom. Auger–Coster-Kronig transition rates were taken from Chen, Crasemann, and Mark [26] for K- and L-shell vacancies, McGuire [27,28] for M-shell vacancies, and McGuire [29] for N-shell vacancies, and when necessary they are reduced or updated according to the current situation of the atom, as follows. If in an Auger transition the shell from which the two active electrons are taken is not full, the rates are multiplied by the sample ratio of the number of available electrons to the number in the full shell. Let us take, for example, the Auger transition where the L_1 vacancy would be filled by an electron from the $M_{2,3}$ shell while an electron from the N_1 shell is emitted. Suppose that the $M_{2,3}$ shell has only four electrons rather than a complete shell of six and the N_1 shell has one electron instead of two. Then the current rate for this transition is obtained multiplying the full shell $L_1M_{2,3}N_1$ rate by the factor $\frac{4}{6}\times\frac{1}{2}$. In the case of a transition, where both electrons come from the same subshell, the ratio of the number of possible pairs is taken. Thus for the $L_1M_{2.3}M_{2.3}$ Auger transition both electrons would originate from the $M_{2,3}$ shell with four electrons and the ratio is 6/15. We further assume that the ion has no memory of the absorbed x-ray direction when the Auger–Coster-Kronig transitions take place so the electron emission direction is assumed to be isotropic.

If an electron makes a transition from an outer shell to an inner vacancy, a photon may be emitted instead of an electron as in Auger–Coster-Kronig transitions. The energy of such fluorescence photons is just the difference in the binding energies of the electrons in the initial and final subshells. Transition rates for fluorescence transitions are given by Scofield [30] for K- or L-shell vacancies and by Manson and Kennedy [31] for M-, N-, and O-shell vacancies. These transition rates are again adjusted, when necessary, for transitions from less than a full shell. Again the distribution of the directions of emission is assumed to be isotropic.

In order to use the Auger–Coster-Kronig or fluorescent decay rates of a particular vacancy in the simulation, they must be converted into probabilities. These probabilities are simply proportional to the magnitude of the current rates. If inner vacancies still exist, either type of transition may occur and all the Auger–Coster-Kronig and fluorescence current rates are considered together to produce a single set of probabilities which are used to describe which particular transition occurs at this stage.

Electron shake-off may occur when an electron is emitted (either through photoionization or an Auger–Coster-Kronig transition) with an energy much greater than the binding energy of the shell from which it came. The sudden change in the effective potential experienced by outer electrons may lead to the ejection of one further electron, the so-called "shake-off" electron. This emitted electron has a relatively low-energy characteristic of the subshell from which it was removed (Carlson and Nestor [32]). Shake-off probabilities following either a photoionization or an Auger–Coster-Kronig transition are taken from [32]. These probabilities were adjusted as outlined above if the shell from which the shake-off electron originates is not full. As with Auger–Coster-Kronig electrons we assume the direction of emission to be isotropic.

III. ELECTRON-SCATTERING CROSS SECTIONS IN XENON

After electrons have been produced by the various processes described in the preceding section, we simulate their movement through the xenon gas under the influence of the applied electric field E, which in the present work is assumed to be uniform. These electrons undergo collisions with the gas atoms and we require both integral and differential scattering cross sections for these collisions in order to determine the path of the electron through the gas and the energy transferred between electrons and gas atoms. Integral cross sections represent the probability of a given process occurring while angular differential cross section will determine the direction of motion of the colliding electron after the collision relative to its direction prior to the collision.

By far the most common type of collision that occurs is an elastic collision. Although there is no energy lost by the electron in such collisions when described in the center-of-mass frame, this is not true in the laboratory frame. In this frame there is a net transfer of energy from electrons to the gas atoms. Low-energy integral and differential cross sections for elastic collisions, $\sigma^{\rm el}(\varepsilon)$ and $d\sigma_\varepsilon^{\rm el}/d\Omega$, are discussed by McEachran and Stauffer [33], Stauffer, Dias, and Conde [34], McEachran and Stauffer [35]. The integral cross sections described in [34] were used in the lower range of electron energies, covering the region of the Ramsauer minimum. Above this our adopted integral elastic cross section follows data from Hayashi [36]. In Fig. 2 our elastic cross section is compared to the data of various other authors. Angular differential cross sections were calculated from the phase shifts described in Stauffer, Dias, and Conde [34] up to 20 eV; see Fig. 3. Above this value we assumed that the shape of the cumulative angular probability distribution $P^{\rm el}(\varepsilon,\theta)$ (shown in Fig. 4) obtained from these differential cross sections (see Sec. IV C) was independent of electron energy [i.e., $P^{\rm el}(\varepsilon>20\text{ eV},\theta)$ equal to $P^{\rm el}(\varepsilon=20\text{ eV},\theta)$].

If the electrons have sufficient energy, either due to their formation via photoionization or cascade processes or by gaining it from the electric field, they can undergo inelastic collisions with the xenon atoms in the gas. These are of two types, viz. excitation where the electron loses an amount of energy necessary to excite the atom to one of its bound electronic states of higher energy, or ionization where in addition to the initial electron losing energy, one or more secondary electrons are produced. Inelastic collisions are of prime importance in the energy degradation of the cascade electrons, until the primary (subionization) electron cloud is fully grown.

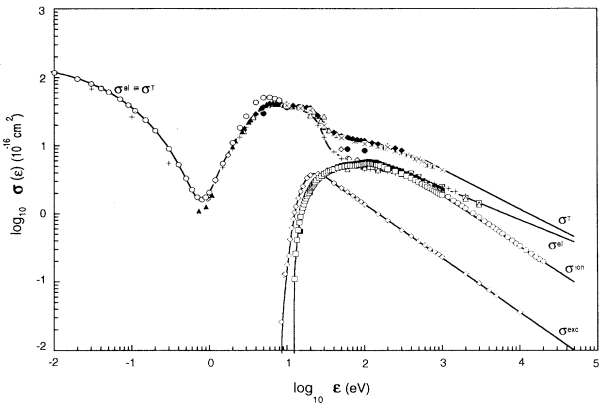

FIG. 2. Electron-impact-scattering cross sections σ^{el} (elastic), σ^{exc} (excitation), σ^{ion} (ionization), and σ^T (total) in xenon. σ^{el}: + Hayashi [36]; ◇ Register, Vuskovic, and Trajmar [37]; ● Haberland, Fritsche, and Noffke [38]; ■ Jansen and de Heer [39]; △ de Heer, Jansen, and van der Kaay [40]; and ● McEachran and Stauffer [35]. σ^{exc}: ◇ Hayashi [41]. σ^{ion}: □ Rapp and Englander-Golden [44]; ○ Schram *et al.* [45], ■ Krishnakumar and Srivastava [46]. σ^T: △ Dababneh *et al.* [48]; * Dababneh *et al.* [49]; ▲ Subramanian and Kumar [50]; ♦ Nickel *et al.* [51]; × Hayashi [36]. Continuous curves are fittings adopted in this work.

There is an infinite number of bound, excited states in an atom, but only a few are of any consequence for the simulation in question. In addition, the probability of an excitation is much smaller than that of an elastic collision or, where energetically possible, of an ionizing collision. Collisions producing excited states are responsible for the scintillation radiation, which is the basis for gas proportional scintillation counters, and we assume that any atom that is excited will eventually lead to the emission of a scintillation photon. Our integral excitation cross section $\sigma^{exc}(\varepsilon)$ is obtained from the data of Hayashi [41] as shown in Fig. 2. Angular differential and partial cross sections for 12 excitation "features" had been reported by Filipovic *et al.* [42] at 11 different energies. From these we have calculated a weighted mean excitation energy ε_{exc} as a function of the electron impact energy ε, which represents the energy lost by the electron during an excitation. However, in some of our simulations (described in Sec. V B) we used instead detailed partial excitation cross sections as recently described in Puech and Mizzi [43] for 12 excited states with energy ε^i_{exc}. Because of the infrequent occurrence of inelastic collisions, accurate angular differential cross sections were not required. We have used a simple straight-line representation of these differential cross sections, $d\sigma^{exc}_{\varepsilon}/d\Omega$, as a function of scattering angle θ. The slope of these lines is a quadratic function of the electron energy ε, with the coefficients chosen to reproduce the integral excitation cross section values from Hayashi [41] and to provide a reasonable fit to the angular scattering data of Filipovic *et al.* [42].

The ionization cross section we use is based on the experimental results of Rapp and Englander-Golden [44] and Schram *et al.* [45], and $\sigma^{ion}(\varepsilon)$ is represented again in Fig. 2. Since no results exist for the differential cross sections in either angle (double) or energy (single) for electron ionization of xenon we have used the shape of the corresponding cross sections for helium measured by Mueller-Fiedler, Jung, and Ehrhardt [47] to calculate the probability distribution for the sharing of the excess electron energy $\varepsilon - \varepsilon_{ion}$ between the two outgoing electrons.

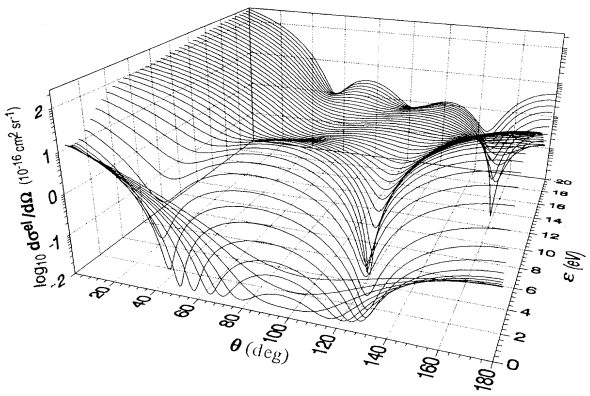

FIG. 3. Angular differential elastic-scattering cross section $d\sigma^{el}/d\Omega$ in xenon for electron-impact energies $\varepsilon \leq 20$ eV (Stauffer, Dias, and Conde [34]).

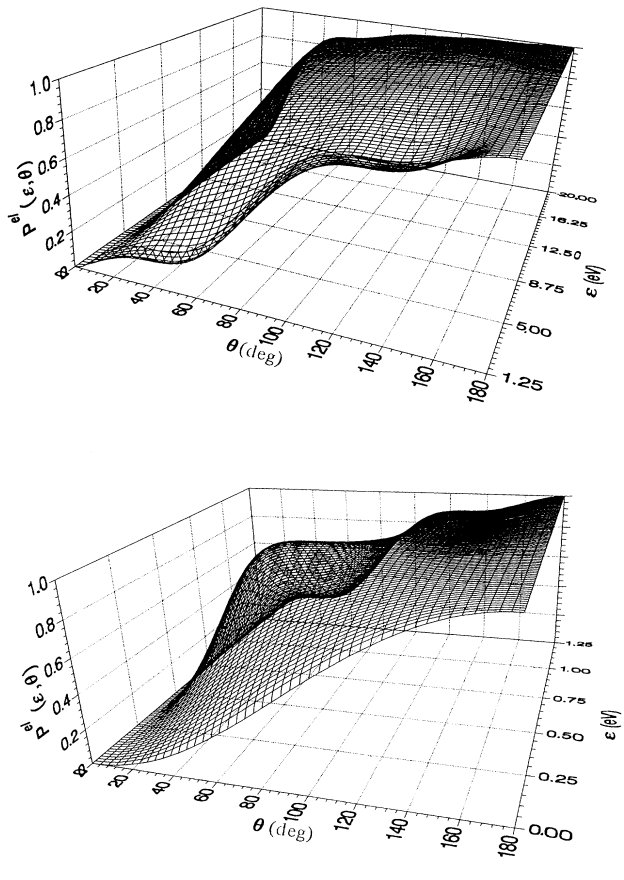

FIG. 4. Cumulative probability surface $P^{el}(\varepsilon,\theta)$ for angular elastic scattering, corresponding to $d\sigma^{el}/d\Omega$ shown in Fig. 3.

Figure 5 displays typical single differential cross sections $d\sigma_{\varepsilon}^{\text{ion}}/d\varepsilon'$ and cumulative probability curves $P_{\varepsilon}^{\text{ion}}(\varepsilon')$ of this type where ε is the electron-impact energy and ε' is the energy of one of the outgoing electrons (the other will be emitted with energy $\varepsilon''=\varepsilon-\varepsilon_{\text{ion}}-\varepsilon'$). Since one electron always has more energy than the other, we assume that the faster electron moves in the same direction as the incident electron after the collision while the direction of the slower one has an isotropic distribution. Although it is possible to produce more than one ejected electron during an ionizing collision, the probability of such an event is small compared to the ejection of a single electron within the electron energy range we considered, and so we assume that the latter situation always occurs.

The sum of the integral elastic, excitation, and ionization cross section produces the total electron-impact scattering cross section $\sigma^{T}(\varepsilon)$, which is used to determine the length of the electron path through the gas. This cross section depends, of course, on the energy ε of the electron. The total scattering cross section is also shown in Fig. 2 and compared to various experimental results. All four electron-impact scattering cross sections in Fig. 2 are represented by cubic spline functions of the electron-impact energy ε, enabling us to calculate the required values at any given point of the simulation.

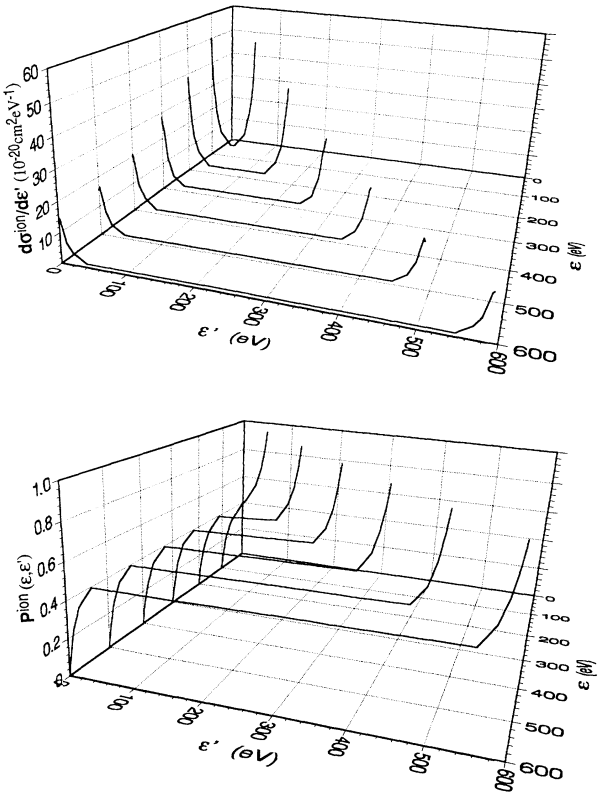

FIG. 5. Single differential cross sections $d\sigma^{\text{ion}}/d\varepsilon'$ and corresponding cumulative probabilities $P^{\text{ion}}(\varepsilon,\varepsilon')$ in xenon as adopted in this work, represented for electron-impact energies $\varepsilon=100$, 200, 300, 400, 500, and 600 eV.

IV. THE SIMULATION MODEL

The simulation can be broken down into a number of separate steps. These involve (i) the photoionization of an atom by the incident x ray or by a fluorescent photon, (ii) the decay of the residual ion via Auger–Coster-Kronig, fluorescence and shake-off transitions, (iii) the ionization of further atoms by impact with fast electrons, and (iv) the drift of the electrons through the gas with the production of scintillation photons and possibly further electrons. The first three steps are involved with the production of the primary-electron cloud while the last step results in the production of scintillation photons and, for high enough applied electric fields, secondary electrons. The details involved in all these steps are summarized in the flow charts on Figs. 6 and 7. In addition we must consider the criteria used to terminate the simulation depending on the required results and the physical situation being modeled, and the means of interpolating the simulation data to extract the physical parameters of interest. Examples of these are described in Sec. V.

A detailed description of the simulation process is

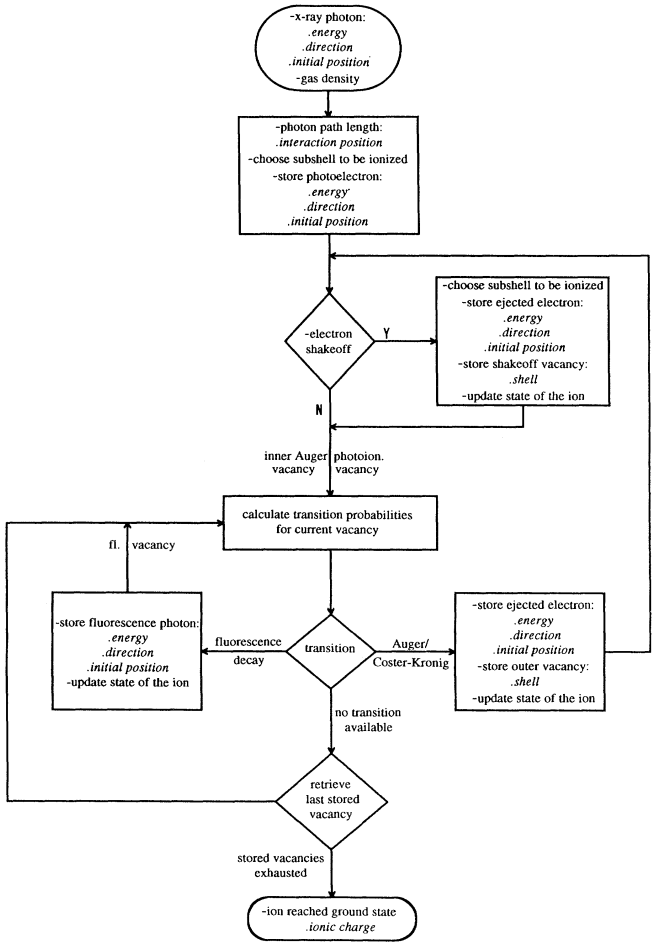

FIG. 6. Simplified flow chart of the Monte Carlo simulation of the interaction between an x-ray photon and a xenon atom and the decay of the ensuing excited xenon ion.

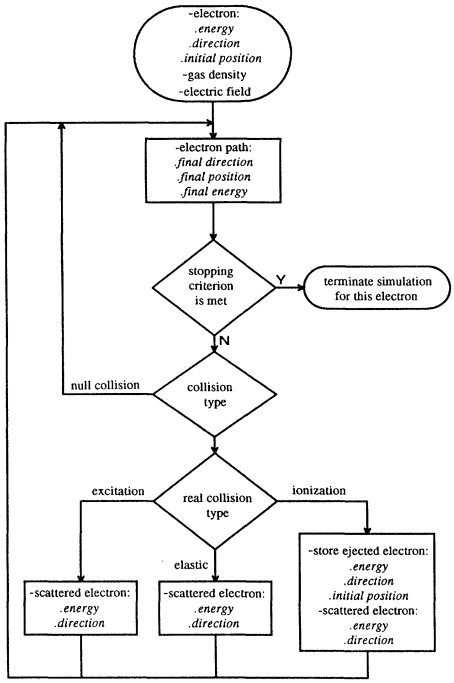

FIG. 7. Simplified flow-chart of the Monte Carlo simulation of the history of one electron.

given below. We assume the reader is familiar with the basics of Monte Carlo simulation and will not go into detail on the generation of random numbers or the choice among possible outcomes based on standard probability distributions.

A. Photoionization

In the study of the interaction of x rays with a gas medium, the absorption of a large number of such x-ray photons (typically 25 000) is simulated. We assume an x ray of known energy E_{xr} that enters the gas parallel to the applied electric field and perpendicular to the entrance window of the detector. We then have to decide at which depth in the gas the x ray interacts with a gas atom and from which subshell the photoelectron is ejected. A similar decision process occurs for each of the fluorescence photons produced in the decay of the residual ion. In the latter case, the direction of travel and energy of the photon has already been determined during the simulation of the fluorescent decay process (see Sec. IV B). The applied electric field plays no role in the photoionization process.

The distance d_{xr} a photon of fixed energy E_{xr} travels through the gas before it is absorbed has an exponential distribution with mean $\bar{d}_{xr}=1/N\sigma_{ph}^{T}(E_{xr})$ where N is the number density of the gas atoms and σ_{ph}^{T} is the x-ray energy-dependent total photoionization cross section. d_{xr} is thus sampled by making $d_{xr}=-\bar{d}_{xr}\ln R=-[1/(N\sigma_{ph}^{T})]\ln R$, where R is a random number chosen from an uniform distribution in the range]0,1[. A penetration distance for the original x ray is randomly chosen from this distribution to give the position $(0,0,z_0)$ of the photon-atom interaction. A further random choice is made among the various subshells of the atom for the origin of the photoelectron based on the relative values at an energy E_{xr} of the partial photoionization cross sections σ_{ph}^{p} for each of the atomic subshells. The ejected photoelectron has energy $\varepsilon_{ph}=E_{xr}-B^{i}$, where B^{i} is the binding energy of the ith subshell of the atom from which the photoelectron originates. The photoelectron is emitted in a direction (θ,ϕ), where θ is chosen from the distribution based on the angular differential cross section for the ith subshell having the form given in Eq. (1) and ϕ is chosen from the uniform distribution on $[0,2\pi]$. The information about the photoelectron (energy, direction, and position) is stored until it is used later as described in Sec. IV C. Information on the current vacancies in the residual ion is also retained.

B. Decay of the residual ion

Unless the photoelectron has come from the outermost subshells of the atom, the residual ion is in an excited state and the photoelectron vacancy will decay via the three processes: Auger–Coster-Kronig transitions, fluorescence photon emission, and shake-off ionization.

Immediately after photoionization, a decision is made as to whether a shake-off electron has been produced and if so, from which subshell it originates, based on the probabilities given in [32]. The information on its energy, direction (from an isotropic distribution; see Sec. II B), and position $(0,0,z_0)$ is stored until needed. The information on the current subshell vacancies in the ion is updated.

At this point a further transition in the ion will normally take place. In order to determine which transition occurs from the various Auger–Coster-Kronig or fluorescence emission series, it is necessary to use the relevant current probabilities calculated as explained in Sec. II B. A specific transition is randomly chosen on the basis of these probabilities.

If the transition chosen is a fluorescent decay, the energy, direction of emission, and initial position $(0,0,z_0)$ of the fluorescent photon are calculated as explained in Sec. II B and this information is stored.

If the transition is an Auger–Coster-Kronig one, the energy of the ejected electron is calculated according to Eq. (2). The direction of ejection is chosen from an isotropic distribution and again this information is stored along with initial position $(0,0,z_0)$ of the electron and its energy. After an Auger–Coster-Kronig transition, a shake-off electron may also be ejected. This possibility is considered in the same manner as after a photoionization as outlined above and the relevant information on the electron is stored.

After any specific transition has taken place, the state of the current electron vacancies in the ion is updated. If there still exists an inner vacancy the decay of this vacancy is simulated by repeating the process described above. When the residual ion has reached its lowest-energy state no further transitions will take place. The exact sequence

of steps is given in Fig. 6. In the end, when no more transitions are available, the residual ion will reach its lowest-energy state, with all vacancies in the three outermost subshells.

Once the residual ion has reached its lowest-energy state its final charge is recorded. However, the effect of the fluorescent photons which have been emitted during the decay still has to be considered. Each of these photons is assumed to photoionize another gas atom. The results of such photoionizations can be calculated in exactly the same manner as for the incident x ray. Only the initial conditions of the photon (energy, direction of travel, initial position) are different from the original incident x ray. Once all of the fluorescent photons have been treated in this manner another x ray from the original set is introduced and the simulation process repeated. Once the set of x-ray photons is exhausted there remains stored a large number of electrons which will now be followed as described in Sec. IV C.

C. Electron-gas interactions

The free electrons move through the gas under the influence of the applied uniform electric field E. The initial conditions of each of these electrons have been stored the moment they were emitted by the atoms and we treat each one in turn, following its progress through the gas until the criterion for ending the current electron history has been reached (see Sec. IV D). Unlike the photons, the electrons are affected by the field, so that their paths are parabolic and their velocities (and hence energies) change continuously along their paths. The formula for the component of electron velocity parallel to the field v_z at a time t after the beginning of the electron trajectory is given by

$$v_z = v_{z0} + eEt/m \ ,$$

where v_{z0} is the component of electron velocity at time $t=0$, e the electron charge, m its mass, and E the strength of the applied electric field. The components perpendicular to the field remain constant. This free path of the electron is terminated when it collides with a gas atom.

The fact that the energy and hence the total scattering cross section σ^T do vary along the path means that the determination of the time between collisions is computationally intensive. However, we can avoid this problem by using the null collision method [52–54]. This method allows us to use a constant collision frequency Γ along the path at the cost of introducing extra collisions (the null collisions) which have no effect on the final results of the simulation. Details of the efficient application of this method are given in Ref. [52]. The time τ between collisions is thus determined by sampling from an exponential distribution with mean $\tau = 1/\Gamma$, i.e., by taking $\tau = -\bar{\tau} \ln R = -1/\Gamma \ln R$, where R is a random number chosen from an uniform distribution between]0,1[.

A decision is made, at each electron impact energy ε, on which type of collision occurs—elastic, excitation, or ionization—depending on the relative magnitudes of the individual integral cross sections. Note that elastic collisions are always possible, but the other two require the electron to have an energy in excess of their respective thresholds: 8.32 eV for excitation, 12.1 eV for ionization.

The cross sections refer to collisions in the center-of-mass frame of reference of the electron-atom pair. Thus in the case of elastic collisions we transform to this frame before determining the direction of travel of the electron after the collision. In the range where inelastic collisions are possible, the energies of the electrons are large compared to the thermal energies of the gas atoms and we remain in the laboratory frame for these collisions. The velocity of the gas atom is randomly chosen from a Maxwellian distribution reflecting the temperature of the gas. The scattering angles of the scattered electron relative to its velocity just prior to the collision are in each case determined from the angular differential cross sections $d\sigma/d\Omega \equiv \sigma(\theta,\phi)$ described in Sec. III. The cumulative probability for the scattering of an electron with energy ε through a polar angle θ is given by

$$P(\varepsilon,\theta) = \int_0^{\infty} \sigma_{\varepsilon}(\theta') \sin\theta' d\theta' \Big/ \int_0^{\pi} \sigma_{\varepsilon}(\theta') \sin\theta' d\theta' \ ,$$

while the azimuthal scattering angle ϕ is chosen from a uniform distribution on $[0,2\pi]$. Note that the angular differential cross section implicitly depends on ε. In order to reduce the computation time, surfaces of $P(\varepsilon,\theta)$ are constructed on a mesh of values of θ and ε, and the particular values required are interpolated from these values. Such surface are used for elastic collisions and excitations. The plot of one of these surfaces, namely $P^{\mathrm{el}}(\varepsilon,\theta)$, is shown in Fig. 4. If the electron energy immediately before a collision is ε and the event is an inelastic one, a new energy ε^s after the collision is calculated as the excess $\varepsilon^s = \varepsilon - \varepsilon_{\mathrm{in}}$, where $\varepsilon_{\mathrm{in}}$ is taken, in the case of ionization or excitation, as the ionization threshold $\varepsilon_{\mathrm{ion}}$ or the excitation energy $\varepsilon_{\mathrm{exc}}$, respectively. If the collision is an ionizing one, an additional electron is produced and the energy ε^s is shared between the two outgoing electrons as described in Sec. III. The position and the velocity of this electron are stored to be considered along with the rest of the free electrons not yet analyzed. At this point a new free path is determined using as initial conditions the velocity and position of the electron immediately after the collision. This process is repeated until the criterion for terminating the electron history is satisfied. Then another electron is treated in the same manner until all the electrons stored have been considered.

D. The stopping criteria

The point at which the simulation terminates depends on the process being studied. We give below the criteria used in the various processes we have studied to date.

For those parameters which involve a knowledge of the growth and final state of the primary-electron cloud, or in other words, those which describe the conversion of the energy of the incident x ray into the primary-electron cloud, the simulation is terminated when all the electrons produced reach an energy below the ionization threshold of xenon. This was the stopping criteria used to investigate the size of the primary-electron cloud [7], the Fano factor F, intrinsic energy resolution R [8], mean energy w

to produce an electron-ion pair, and the intrinsic energy linearity of the average number of primary electrons produced per x ray [9].

In our study of spectral distortion due to the presence of the entrance window [10,11], the history of each electron ends either when it hits the window or it reaches a position from which it is energetically impossible to return to the window.

We have also calculated several parameters characteristic of the drift of primary electrons under the influence of the electric field in xenon, namely electron-drift velocity and mobility, diffusion coefficients, and characteristic energies in the gas, as well as some xenon scintillation parameters such as excitation and scintillation efficiencies, reduced light output, distance between luminous layers, number of elastic collisions, and elapsed time between successive excitation collisions [12,13]. For all these calculations, we allowed the sample of electrons considered to drift for a time long enough so that these parameters reached, in each case, an equilibrium value in the applied electric field.

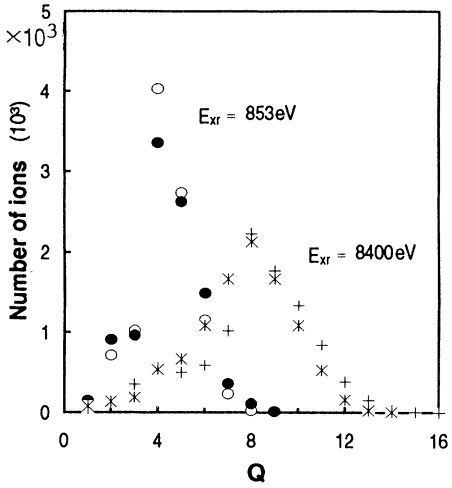

FIG. 8. Charge distribution of xenon ions produced by the absorption of 10^4 x-ray photons with energies $E_{xr}=853$ and 8400 eV: ●, * Carlson, Hunt, and Krause [55]; ○, + this work.

V. RESULTS OF THE SIMULATIONS

We will now summarize in more detail how the various parameters are obtained from the simulation data and present some typical results. More extensive results are in general given in our papers [5–13]. Throughout all these simulations we have assumed a temperature of 293 K and a xenon pressure of 760 Torr.

In Sec. V A we will present results which essentially were obtained with simulations starting with a sample of x-ray photons absorbed in xenon, following, whenever required, the final primary (subionization) electrons in their drift in the gas, whereas in Sec. V B we look into another group of results corresponding to simulations which were directly initiated with a sample of electrons.

A. X-ray photon simulation

Starting with a sample with not less than 10 000 x-ray photons of fixed energy E_{xr}, in a first stage of the work we have calculated the charge distribution of the xenon ions resulting from the absorption of the x rays [5,6] using the cascade decay scheme described in Sec. II. A careful modeling of the vacancy cascade decay of the excited photoionized xenon ion is very important, as the resulting emitted electrons, together with the photoelectron, constitute the initial source which produces the primary-electron cloud, thus affecting all results involving the final group of primary electrons. In Figs. 8–10 we present examples of xenon charge distributions yielded by the present simulation, showing good agreement with published data [55–58]. Moreover, we tested our decay scheme by calculating the ion charge distribution after internal conversion following radiative decay in xenon, to compare it with experimental [59] and earlier Monte Carlo results [23]. Good agreement was also obtained in this case as shown in Fig. 11.

The size and shape of the primary-electron cloud which develops after x-ray absorption is an intrinsic limit to the spatial resolution of position sensitive gaseous detectors, therefore we have investigated the spatial density distribution of primary electrons [7]: some typical results are shown in Fig. 12 for the range of x-ray energies studied. We can observe that as the x-ray energy increases, the cloud extends to larger radial distances, with a broad maximum gradually emerging and shifting to the right. This maximum was found to correspond to the contribution of the primary electrons arising from the initial photoelectrons, whose energy increases in general with x-ray energy. By selecting, in the Monte Carlo

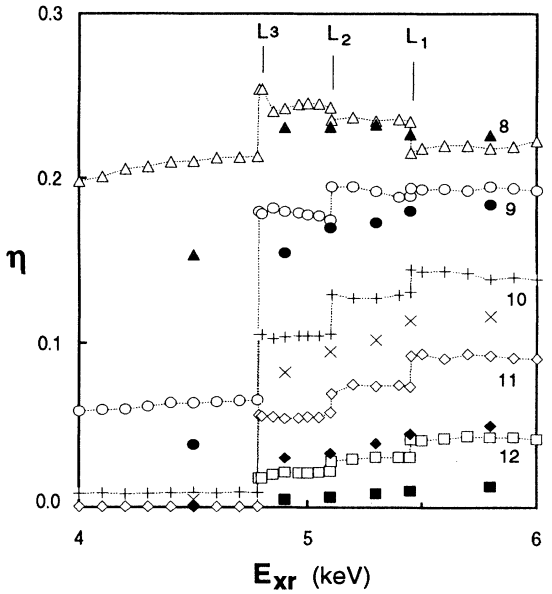

FIG. 9. Fraction η of xenon ions with charges from 8 to 12 as a function of absorbed x-ray energy E_{xr} near the L absorption edges: ▲,●, ×, ◆, ■ Mukoyama *et al.* [56], Tawara *et al.* [57], experimental; △, ○, +, ◇, □ this work.

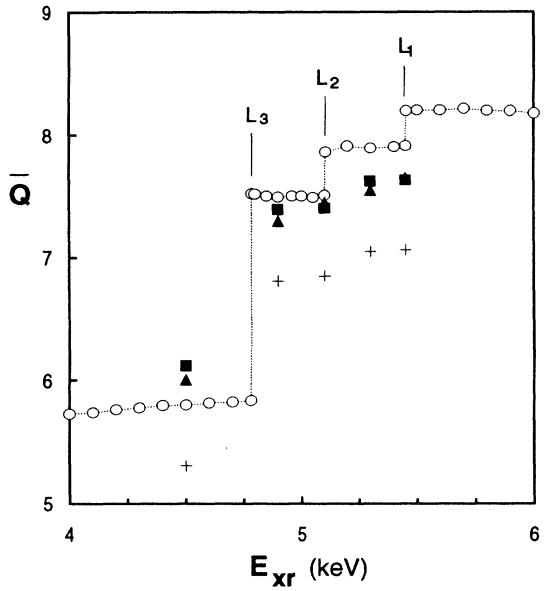

FIG. 10. Mean xenon ion charge $\bar{Q}$ as a function of absorbed x-ray energy E_{xr} near the L absorption edges; + Carlson, Hunt, and Krause [55], semiempirical; ▲ Tonuma *et al.* [58], Monte Carlo; ■ Tonuma *et al.* [58], Tawara *et al.* [57], experimental; ○ this work.

simulation, only the Auger electrons we found them to be the main contributors to the central part of the primary electron cloud; this is to be expected since they tend to have a lower and constant energy distribution (except when a new atomic subshell can be photoionized). In addition, fluorescence emission becomes more important with increasing x-ray energy (above the L edge), but the long tail at large radial distances which corresponds to that effect contains only a small percentage of the total number of primary electrons. In general we conclude that, for the x-ray energy range studied, the size of the primary-electron cloud is below the experimental resolution obtained with position-sensitive detectors for the lower energies. However, for energies higher than 30 keV it reaches sizes that cannot be neglected when spatial resolutions of the order of 1 mm are required [60].

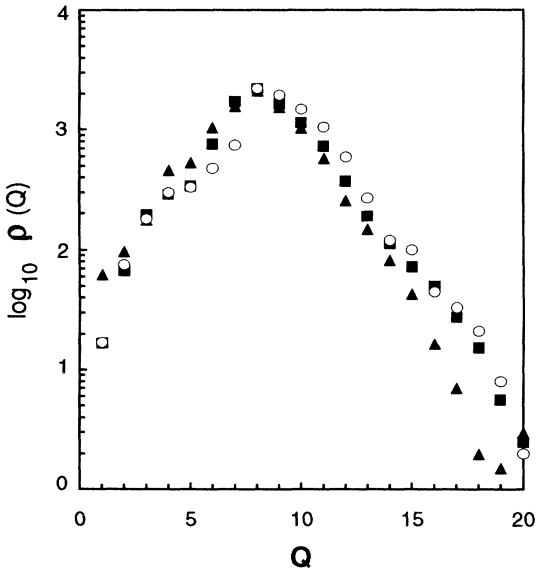

FIG. 11. Xenon-ion charge distribution as a result of the internal conversion following the decay of $^{131}Xe^{m}$ (10^4 ions): ▲ Pleasonton and Snell [59], experimental; ■ Mukoyama [23], Monte Carlo; ○ this work.

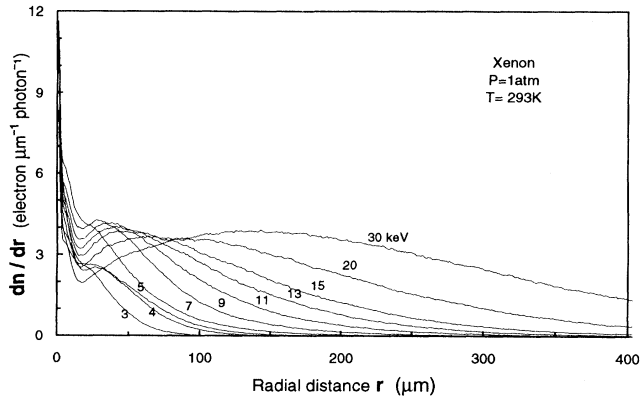

FIG. 12. Electron radial distribution dn/dr as a function of the radial distance r in the primary electron cloud produced in Xe by x rays with energies in the range 3–30 keV.

A very important characteristic of gaseous detectors is their energy resolution, which is limited by the variance in the number n of primary electrons produced by the absorbed photons of a given energy E_{xr}. This variance is lower than the mean number $\bar{n}$ by a factor F, the so-called Fano factor, characteristic of the gas:

$$\sigma_n^2 = F\bar{n} \ .$$

The intrinsic energy resolution of a detector [full width at half maximum (FWHM)] is therefore given by

$$R\,(\%) = 235.5(F/\bar{n})^{1/2} = 235.5(Fw/E_{xr})^{1/2} \ ,$$

where $w = E_{xr}/\bar{n}$ is the mean energy required to produce an electron-ion pair.

With our Monte Carlo simulations, we were able to analyze the behavior of R, F, and w with varying x-ray energy [8,9]. In Table I we list a series of values obtained for these three quantities where the Fano factor and w were calculated directly from the simulation and R was obtained from the FWHM of the Gaussian fits to the calculated spectra (the corresponding spots can be found in Figs. 1 and 3 in Ref. [8] and Fig. 3 in Ref. [9]). Although commonly assumed to be constant, the Fano factor and the w value were found to be x-ray energy dependent, with discontinuities clearly arising whenever the absorbed x-ray energy reaches a value just high enough to allow for a new (inner) atomic subshell to be photoionized. The nature of the dependence of F, w, and R on the x-ray energy, together with their sensitivity to the shell structure of the absorbing gas, was fully explained by our simulation analysis, which enables us to scrutinize the

contributions of all aspects of the processes involved. In spite of the fact that in previous experimental GPSC work clear discontinuities in energy resolution had already been observed apparently pointing to an energy-dependent Fano factor [61], and, likewise, distinct breaks in energy linearity had also been reported in [62–64], these effects had not been fully understood prior to our work. Moreover, the magnitude of the discontinuities in energy linearity which our simulations produced [9] [examined here in Figs. 13(a)–13(d) for x-ray energies close to the $M_{4,5}$ and L_3 absorption edges], are in excellent agreement with the observed experimental values [63,64]. Also, some nonlinearity effects observed in another type of x-ray detector, a low-pressure gaseous detector based on electron counting, have also been attributed in part to the energy dependence of the w values which we have demonstrated [65].

The distortion observed in soft-x-ray energy spectra [66–69] was another important topic thoroughly investigated by our simulation work [11]. It was found that this effect could be fully accounted for by the loss of electrons to the entrance window of the detector when the x-ray penetration depth is small. The detailed Monte Carlo simulation study we have carried out in the $E_{xr}=0.1-5$-keV range [11] has provided a full assessment of the influence of the applied electric field in the x-ray absorption zone in minimizing the degradation of soft-x-ray spectra. As an illustrative example, we show in Fig. 14 a series of spectra calculated at different electric fields in the case of $E_{xr}=715$-eV x rays, which at $P=1$ atm and $T=293$ K have a mean path length $\bar{d}_{xr}$ in the gas [$\bar{d}_{xr}=1/N\sigma_{ph}^{T}(E_{xr})$] equal to 111.8 μm. These spectra are compared with the reference spectrum which was obtained neglecting electron losses: with increasing electric-field strength the successive spectra get closer to the reference spectrum, reflecting the gradual improvement in the collection of electrons.

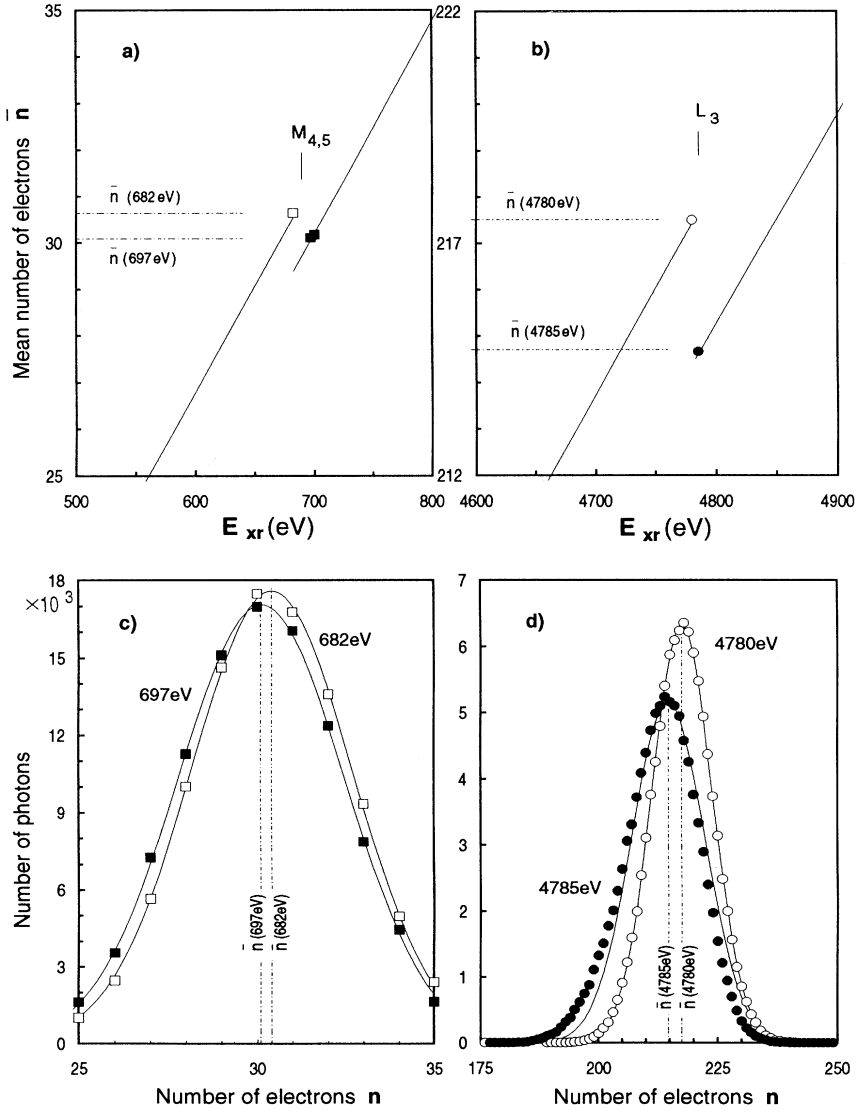

FIG. 13. Calculated number of electrons produced when 10^5 x-ray photons with energy E_{xr} (□, 682 eV; ■, 697 eV; ○, 4780 eV; ●, 4785 eV) are absorbed in xenon. In (a) the break in energy linearity near the $M_{4,5}$ absorption edge (683 eV) is shown, similarly in (b) for E_{xr} near L_3 (4782 eV). The straight lines are the linear fits to the various calculated points at lower and higher energies (not shown). In (c) and (d) the energy spectra belonging to the points represented in (a) and (b) are shown, where the continuous curves are Gaussian fits to the calculated points (spectra are obtained as frequency plots of the number of primary electrons produced by the absorbed x-ray photons). The spectra in (c) and (d) reveal that notwithstanding the fact that E_{xr} increases between (□) 682 and (■) 697 eV, as well as between (○) 4780 and (●) 4785 eV, a clear shift of the mean number of produced electrons to a lower value is evident in both cases, causing the energy linearity breaks shown in (a) and (b).

B. Electron-drift simulations

In parallel with the results obtained when starting with a sample of x-ray photons absorbed in xenon (which were summarized in Sec. V A), a second group of results was obtained by directly "injecting" into the gas a sample of electrons (typically 2500) with zero or low initial energy, which are then allowed to drift in the gas at various E/N values. For these simulations a more recent and detailed set of excitation cross sections described in Puech and Mizzi [43] has been used, and the possibility of the excitation of the 12 discrete excited states considered there was included. Various transport parameters for electrons in xenon were obtained, such a drift velocity v_d, mobility $\mu = v_d/E$, characteristic energies $\varepsilon_{kl} = eD_l/\mu$, and $\varepsilon_{kt} = eD_t/\mu$ with D_l and D_t the longitudinal and transverse diffusion coefficients, together with mean electron energies and distribution functions. The electron drift velocity v_d and the diffusion coefficients were calculated according to the definitions

$$v_d = \frac{d\bar{z}}{dt}, \quad D_l = \frac{1}{2}\frac{d(\overline{z^2} - \bar{z}^2)}{dt}, \quad D_t = \frac{1}{4}\frac{\overline{dr^2}}{dt}$$

using the slopes of the linear variation of the electron ensemble averages $\bar{z}$, $\overline{z^2} - \bar{z}^2$, and $\overline{r^2}$ with elapsed drift time t. Here z is the electron position in the direction of the

TABLE I. Mean energy to produce an electron-ion pair w, Fano factor F, and energy resolution R as a function of absorbed x-ray energy E_{xr} in gaseous xenon.

E_{xr} (eV)	w (eV)	F	R (%)
213	24.00	0.193	34.9
300	23.46	0.188	28.4
500	22.70	0.178	21.3
600	22.53	0.174	19.0
682	22.42	0.169	17.5
697 (M_{45}^+)	23.14	0.181	18.3
700	23.19	0.183	18.2
900	22.91	0.183	16.0
970	22.78	0.184	15.4
971 (M_{23}^+)	23.14	0.209	16.6
978	23.17	0.221	17.0
1 000	23.01	0.213	15.8
1 100	22.91	0.211	15.5
1 147	22.88	0.211	15.1
1 147 (M_1^+)	22.87	0.209	15.5
1 156	22.99	0.231	15.3
1 200	22.95	0.234	15.1
1 500	22.72	0.229	13.5
2 000	22.46	0.213	11.4
3 000	22.20	0.197	9.0
4 000	22.05	0.192	7.5
4 500	22.01	0.187	7.1
4 780	21.98	0.184	6.8
4 785 (L_3^+)	22.36	0.290	8.3
5 000	22.38	0.297	8.3
5 100	22.35	0.292	8.2
5 105 (L_2^+)	22.42	0.303	8.4
5 150	22.43	0.301	8.4
5 200	22.42	0.301	8.3
5 400	22.39	0.296	8.1
5 452	22.45	0.314	8.3
5 453 (L_1^+)	22.45	0.311	8.4
5 480	22.46	0.318	8.3
6 000	22.38	0.304	7.8
7 000	22.24	0.282	7.0
8 000	22.14	0.266	6.3
9 000	22.06	0.256	5.8
10 000	22.00	0.240	5.3

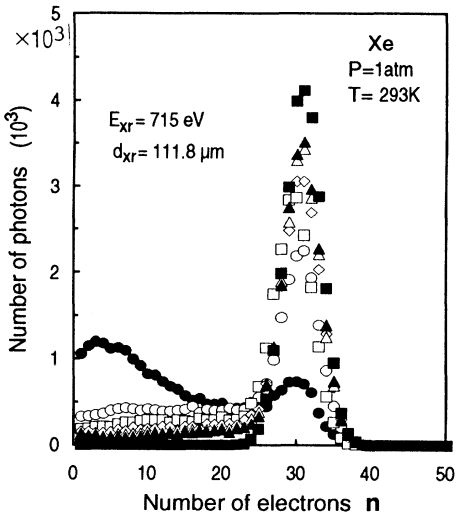

FIG. 14. Effect of the losses to the entrance window on the 715-eV x-ray energy spectra when 25 000 photons are absorbed in xenon, for differential applied electric fields: ●, $E=100$ V/cm; ○, $E=500$ V/cm; □, $E=1000$ V/cm; ◇, $E=1500$ V/cm; △, $E=2000$ V/cm; ▲, $E=2500$ V/cm; and ■, reference spectrum ($E=100$ V/cm, electron losses neglected).

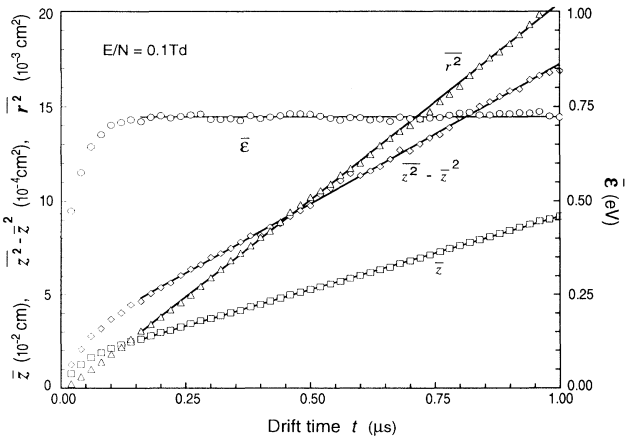

FIG. 15. Variation of the electron ensemble averages $\bar{\varepsilon}$, $\bar{z}$, $\overline{z^2} - \bar{z}^2$, and $\overline{r^2}$ along elapsed drift time t.

electric field ($z=0$ being the release point of the electrons at $t=0$) and r its radial coordinate perpendicular to the electric field. A representative example is shown in Fig. 15, for the case of a reduced electric field $E/N=0.1$ Td. The drift time limit $t_{\rm lim}$ for each simulation was always selected according to the observed evolution with elapsed drift time t: for each E/N considered, $t_{\rm lim}$ was kept as short as possible to save computing time, while guaranteeing that $\bar{\varepsilon}$ had reached an approximately constant value, and that similarly $\bar{z}$, $\overline{z^2}-\bar{z}^2$, and $\overline{r^2}$ exhibited an average linear dependence on t, in order to guarantee that results are obtained when equilibrium with the electric field is reached. As is clear in the example of Fig. 15, a transient nonequilibrium behavior may be visible at very low t (open symbols), and therefore in this case and in any similar one, transport parameters were obtained neglecting this initial phase (relaxation time).

In Figs. 16–20 we present our simulation results for drift velocity v_d, mobility μ, characteristic energies ε_{kl} and ε_{kt}, diffusion coefficients D_l and D_t, and mean electron energy $\bar{\varepsilon}$. Where data were available from the literature we compare our calculated values with either experimental or Boltzmann analysis results. As shown from Figs. 16–20 we have obtained very good agreement in every case.

In addition, for the xenon scintillation range ($E/N\sim 3-16$ Td) we present various other parameters which we have investigated, related to the electroluminescence in xenon, which are of special interest for gas proportional scintillation counters [12,13]. In these calculations it was assumed that for every xenon atom excited, a vuv scintillation photon with energy $\varepsilon_{\rm sci}=7.2$ eV was emitted (at $P=760$ Torr, the xenon continuum emission is peaked at 7.2 eV [80]).

Total excitation and scintillation efficiencies $Q_{\rm exc}$ and $Q_{\rm sci}$ were calculated as

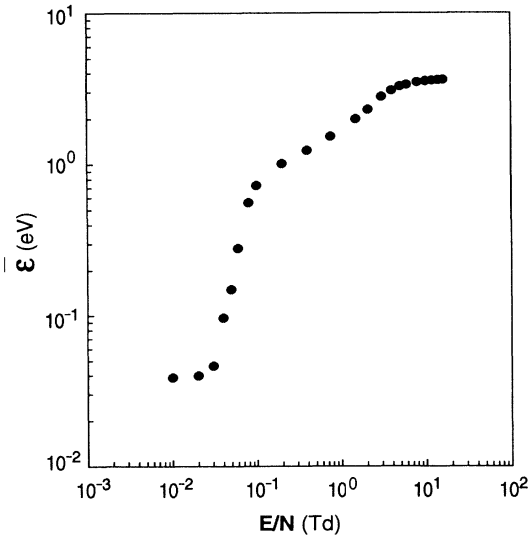

FIG. 16. Mean energy $\bar{\varepsilon}$ of electrons in Xe as a function of reduced electric field E/N.

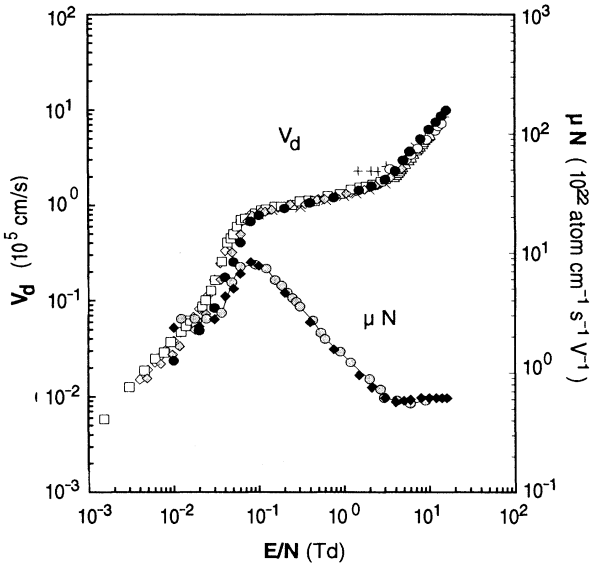

FIG. 17. Electron drift velocity v_d and mobility μN in Xe as a function of E/N: △ Bowe [70]; □ Pack, Voshall, and Phelps [71] and Dutton [72]; ◈, ⊛ Huang and Freeman [73]; ○ Cumpstey and Vass [74]; + Brooks *et al.* [75]; ◇ Hunter, Carter, and Christophorou [76]; × Hashimoto and Nakamura [77]; ●,♦ this work.

$$Q_{\rm exc}=\sum_{i=1}^{12} Q^i_{\rm exc} \quad \text{where } Q^i_{\rm exc}=\sum_{j=1}^{n} n^i_j \varepsilon^i_{\rm exc} \Big/ \sum_{j=1}^{n} eEz_j \ ,$$

$$Q_{\rm sci}=\sum_{i=1}^{12} Q^i_{\rm sci} \quad \text{where } Q^i_{\rm sci}=\sum_{j=1}^{n} n^i_j \varepsilon_{\rm sci} \Big/ \sum_{j=1}^{n} eEz_j \ .$$

The ratios $Q_{\rm exc}$ and $Q_{\rm sci}$ represent the fraction of the energy $\sum_{j=1}^{n} eEz_j$ gained by electrons from the applied elec-

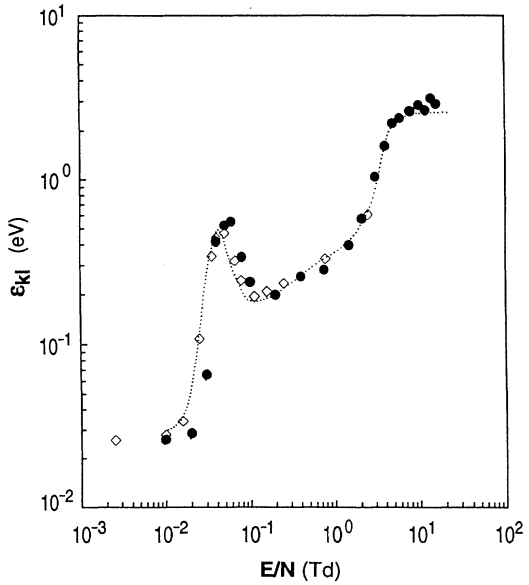

FIG. 18. Characteristic energy $\varepsilon_{kl}=eD_l/\mu$ for electrons in Xe as a function of E/N: ◇ Lowke and Parker [78], and Dutton [72]; · · · · Suzuki *et al.* [4]; ● this work.

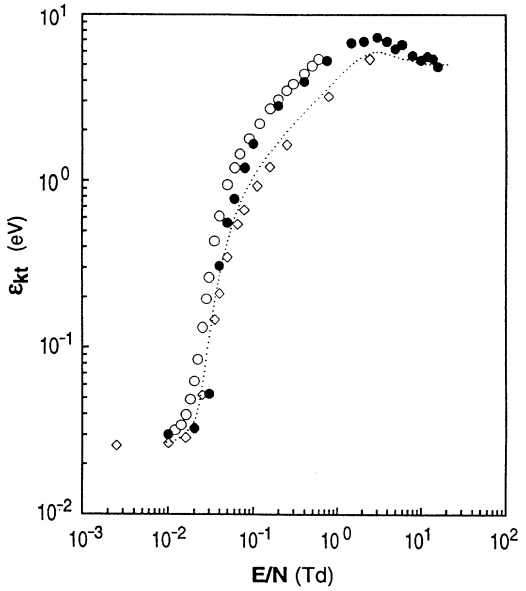

FIG. 19. Characteristic energy $\varepsilon_{kt}=eD_t/\mu$ for electrons in Xe as a function of E/N: ◇ Lowke and Parker [78] and Dutton [72]; ○ Koizumi, Shirakawa, and Ogawa [79]; .... Suzuki *et al.* [4]; ● this work.

tric field E that is used to produce excitation or scintillation. Here n is the number of electrons in the sample, z_j is the distance traveled by electron j during the selected drift time, $\varepsilon_{\rm exc}^i$ is the energy of the ith atomic excited level ($i=1,\ldots,12$), and n_j^i is the number of excitations to the atomic level i produced by electron j.

The xenon reduced light yield Y/N, defined as the average number of vuv photons produced by one electron per unit length and unit density, was calculated as the ratio

$$Y/N=(1/N)\left[\sum_{j=1}^{n} n_j \Big/ \sum_{j=1}^{n} z_j\right] \quad \text{where } n_j=\sum_{i=1}^{12} n_j^i$$

and showed a linear increase with E/N which could be described by

$$Y/N\ (10^{-19}\ \text{photons electron}^{-1}\ \text{cm}^2\ \text{atom}^{-1})$$
$$=(13.89E/N-40.20)\pm 3.28$$

above a scintillation threshold at $E/N=2.89$ Td, which is very close to the experimental value [81,82]. For E/N larger than ~18 Td, the simulations showed the xenon ionization started to occur, confirming experimental results for the ionization threshold [81,82] (Y/N is expected to deviate from the linear behavior described above at higher electric fields due to electron multiplication).

Other characteristic parameters of interest for gaseous scintillation detectors have been calculated, together with their statistical fluctuations, namely the average distance, time interval, and number of elastic collisions between successive excitations. These parameters, as well as the calculated excitation and scintillation efficiencies and reduced light yield, are listed in Table II. We observe that for the larger reduced fields the efficiency for conversion of electrical into optical (scintillation) energy is close to 80%, which might be of practical importance in the production of high-efficiency vuv sources; on the other hand, the large number of elastic collisions between successive inelastic collisions (which produce the scintillation pho-

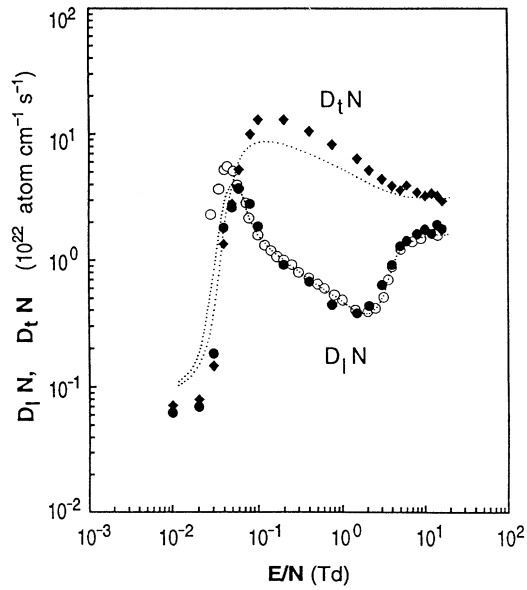

FIG. 20. Longitudinal and transverse diffusion coefficients D_lN and D_tN for electrons in Xe as a function of E/N: ○ Hashimoto and Nakamura [77]; · · · · Suzuki *et al.* [4]; ●,◆ this work.

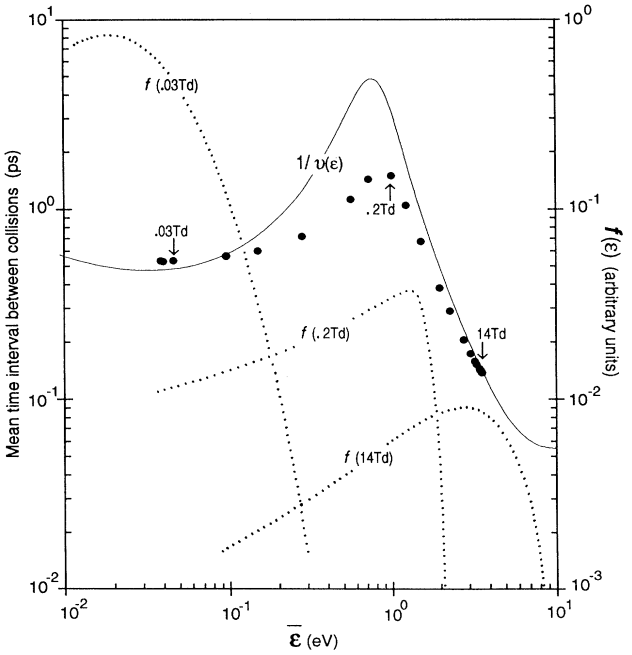

FIG. 21. Mean time interval between electron–Xe-atom collisions: ● Monte Carlo simulation, $-1/\upsilon(\varepsilon)$. The electron energy distribution functions $f(\varepsilon)$ for $E/N=0.03$, 0.2, and 14 Td from Monte Carlo simulation are also outlined.

TABLE II. Electroluminescence parameters in gaseous xenon as a function of E/N.

		Excitation and scintillation efficiencies		Reduced light yield Y/N	Reduced average distance and time, and average number of elastic collisions between successive excitation collisions		
E/N (Td)	E/p_{293} (V cm^{-1} Torr^{-1})	Q_{exc} (%)	Q_{sci} (%)	(10^{-19} photons electron^{-1} cm^2 atom^{-1})	$\Delta Z_L N$ (10^{16} atom cm^{-2})	$\Delta T_L N$ (10^{11} s atom cm^{-3})	ΔN_L (10^3 elastic collisions)
2.00	0.66	0.05	0.04	0.01±0.21			
3.00	0.99	5.30	4.59	1.73±2.36	89.30±33.00	44.00±57.67	857.80±1132.00
4.00	1.32	26.90	23.28	11.08±8.28	31.40±7.64	19.86±15.72	460.55±368.72
5.00	1.65	48.68	42.11	27.29±8.89	24.20±4.67	14.32±9.48	353.7±226.12
6.00	1.98	63.44	54.86	44.52±6.41	17.10±3.02	7.09±3.77	183.44±93.27
8.00	2.64	78.60	67.84	74.76±4.14	12.10±0.90	2.85±0.74	77.98±18.91
10.00	3.30	85.96	73.98	102.41±2.84	9.12±0.59	1.62±0.30	45.34±7.91
12.00	3.96	90.08	77.20	128.50±2.08	7.49±0.38	1.07±0.15	30.18±3.94
14.00	4.46	92.68	79.07	153.68±1.37	6.60±0.47	0.76±0.07	21.80±2.01
16.00	5.26	94.20	80.00	177.37±1.65	5.49±0.23	0.58±0.06	16.82±1.64

tons) emphasizes the importance of the gas purity. The spacing between periodic excitation regions (the so-called luminous layers [83]) is also exhibited in our results, a spacing which is seen to decrease with increasing E/N, i.e., with the increasing excitation efficiency.

In Fig. 21 we present the calculated mean time interval between electron-xenon collisions, calculated for a series of increasing E/N values, versus the corresponding calculated mean electron energy $\bar{\varepsilon}$. The maximum located near 1 eV is related to the minimum in the electron collision frequency $\nu(\varepsilon)=\sigma(\varepsilon)N\nu$ (ν is the electron velocity) due to the Ramsauer minimum in the scattering cross section $\sigma^{el}(\varepsilon)$ (located at $\sim$0.8 eV).

In Fig. 21 we illustrate the fact that in this region the simulation values differ substantially from the corresponding $1/\nu(\varepsilon=\bar{\varepsilon})$ values, which are represented by the solid line. Since near the Ramsauer minimum electrons have very long free paths and the collision frequency varies very rapidly, the energy distributions tend to be very broad, and therefore the mean electron energy will not provide a reliable measure for the general behavior. To illustrate this, some calculated electron energy distributions are also given in Fig. 21, at some typical E/N values (very low, 0.03 Td; intermediate E/N allowing for electron energies near the Ramsauer minimum, 0.2 Td; above the scintillation threshold, 14 Td).

Finally we would like to comment on the earlier calculations where a unidimensional model was used to calculate some electroluminescence and drift parameters in noble gases [14]. Where there were common results, a detailed comparison with the present three-dimensional simulations is made in [13]. However, we can say that above $\sim$11 Td these results tend to deviate from the expected behavior, namely drift velocities are too low, and light yields do not show linear behavior. This is attributed to the simplicity of the unidimensional approach and to the crudeness of the inelastic-scattering cross sections adopted in that work.

VI. CONCLUSIONS

In this paper we have described in detail our Monte Carlo simulation model which we have used to study the characteristics of xenon-filled gaseous detectors and the physics of the processes involved. A number of typical results have been presented which show the power of the Monte Carlo method in being able to model detailed atomic processes which occur in these detectors. Our results have led to a more complete understanding of the behavior of such detectors and how they can be operated in an optimal manner. Further work is already under way, namely the extension of our work to the case of xenon-filled proportional counters. Also planned is a study of the influence of the position and depth of the Ramsauer minimum on the values of electron transport parameters, as well as a study of electron relaxation time.

ACKNOWLEDGMENTS

This work was supported by Instituto Nacional de Investigação Científica, Portugal; Junta Nacional de Investigação Científica e Tecnológica, Portugal; Laboratório Nacional de Engenharia e Tecnologia Industrial, Portugal, through Eureka Project No. EU-39; and Natural Sciences and Engineering Research Council, Canada. Special thanks are due to Professor Eugene J. McGuire for valuable help in the earlier stages of this work.

[1] Glenn F. Knoll, *Radiation Detection and Measurement* (Wiley, New York, 1979).

[2] W. P. Allis, in *Motions of Ions and Electrons,* edited by S. Flügge, Handbüch der Physik Vol. XXI (Springer-Verlag, Berlin, 1956), p. 383.

[3] L. G. H. Huxley and R. W. Crompton, *The Diffusion and Drift of Electrons in Gases* (Wiley, New York, 1974).

[4] M. Suzuki, T. Taniguchi, N. Yoshimura, and H. Tagashira, J. Phys. D **25**, 50 (1992).

[5] F. P. Santos, T. H. V. T. Dias and C. A. N. Conde (unpub-

lished).

[6] F. P. Santos, T. H. V. T. Dias, and C. A. N. Conde, in *Proceedings of the Symposium on Atomic and Surface Physics, Trentino, Italy, 1992,* edited by D. Bassi, M. Scotoni, and P. Tosi (Universita di Trento, Trento, 1992), p. 2.97.

[7] T. H. V. T. Dias, F. P. Santos, and C. A. N. Conde, Nucl. Instrum. Methods A **310**, 137 (1991).

[8] T. H. V. T. Dias, F. P. Santos, A. D. Stauffer, and C. A. N. Conde, Nucl. Instrum. Methods A **307**, 341 (1991).

[9] F. P. Santos, T. H. V. T. Dias, A. D. Stauffer, and C. A. N. Conde, Nucl. Instrum. Methods A **307**, 347 (1991).

[10] F. P. Santos, T. H. V. T. Dias, A. D. Stauffer, and C. A. N. Conde, in *Summary Transactions of the 5th International Symposium on Radiation Physics, Dubrovnik, Croatia, 1991,* edited by A. Ljubicic (Ruder Boskovic Institute, Zagreb, 1991), p. ii-23.

[11] T. H. V. T. Dias, F. P. Santos, A. D. Stauffer, and C. A. N. Conde, Phys. Rev. A **46**, 237 (1992).

[12] F. P. Santos, T. H. V. T. Dias, A. D. Stauffer, and C. A. N. Conde, in *Proceedings of the 10oh International Conference on VUV Radiation Physics, Paris, 1992,* edited by Y. Petroff (Maison de la Chimie, Paris, 1992), p. mo-82.

[13] F. P. Santos, T. H. V. T. Dias, A. D. Stauffer, and C. A. N. Conde (unpublished).

[14] T. H. V. T. Dias, A. D. Stauffer, and C. A. N. Conde, J. Phys. D Appl. Phys. **19**, 527 (1986).

[15] M. Kutzner, V. Radojevic, and H. P. Helly, Phys. Rev. A **40**, 5052 (1989).

[16] I. M. Band, Yu. I. Kharitonov, and M. B. Trzhaskovskaya, At. Data Nucl. Data Tables **23**, 443 (1979).

[17] D. J. Kennedy and S. T. Manson, Phys. Rev. A **5**, 227 (1972).

[18] J. B. West and J. Morton, At. Data Nucl. Data Tables **22**, 106 (1978).

[19] F. Wuilleumier, Phys. Rev. A **6**, 2067 (1972).

[20] E. B. Saloman, J. H. Hubbell, and J. H. Scofield, At. Data Nucl. Data Tables **38**, 1 (1988).

[21] F. P. Larkins, At. Data Nucl. Data Tables **20**, 319 (1977).

[22] W. M. Veigele, At. Data Nucl. Data Tables **5**, 51 (1973).

[23] T. Mukoyama, J. Phys. Soc. Jpn. **55**, 3054 (1986).

[24] M. O. Krause and T. A. Carlson, Phys. Rev. **158**, 18 (1967).

[25] W. A. Coghlan and R. E. Clausing, Surf. Sci. **33**, 411 (1972).

[26] M. H. Chen, B. Crasemann, and H. Mark, At. Data Nucl. Data Tables **24**, 13 (1979).

[27] E. J. McGuire, Sandia National Laboratories, Report No. SC-RR-71 0835, 1972 (unpublished).

[28] E. J. McGuire, Phys. Rev. A **5**, 1052 (1972).

[29] E. J. McGuire, Sandia National Laboratories, Report No. SAND-75-0443, 1975 (unpublished).

[30] J. H. Scofield, At. Data Nucl. Data Tables **14**, 121 (1974).

[31] S. T. Manson and D. F. Kennedy, At. Data Nuc. Data Tables **14**, 111 (1974).

[32] T. A. Carlson and C. W. Nestor, Phys. Rev. A **8**, 2887 (1973).

[33] R. P. McEachran and A. D. Stauffer, J. Phys. B **19**, 3523 (1986).

[34] A. D. Stauffer, T. H. V. T. Dias, and C. A. N. Conde, Nucl. Instrum. Methods A **242**, 327 (1986); **256**, 406(E) (1987); **261**, 610 (1987).

[35] R. P. McEachran and A. D. Stauffer, J. Phys. B **20**, 3483 (1987).

[36] M. Hayashi, Nagoya University Report No. IPPJ-AM-19, 1981 (unpublished).

[37] D. F. Register, L. Vuskovic, and S. Trajmar, J. Phys. B **19**, 1685 (1986).

[38] R. Haberland, L. Fritsche, and J. Noffke, Phys. Rev. A **33**, 2305 (1986).

[39] R. H. Jansen and F. J. de Heer, J. Phys. B **9**, 213 (1976).

[40] F. J. de Heer, R. H. J. Jansen, and W. van der Kaay, J. Phys. B **12**, 979 (1979).

[41] M. Hayashi, J. Phys. D **16**, 581 (1983).

[42] D. Filipovic, B. Marinkovic, V. Pejcev, and L. Vuskovic, Phys. Rev. A **37**, 356 (1988).

[43] V. Puech and S. Mizzi, J. Phys. D **24**, 1974 (1991).

[44] D. Rapp and P. Englander-Golden, J. Chem. Phys. **43**, 1464 (1965).

[45] B. L. Schram, F. J. de Heer, M. J. V. D. Wiel, and J. Kistemaker, Physica **31**, 94 (1965).

[46] E. Krishnakumar and K. Srivastava, J. Phys. B **21**, 1055 (1988).

[47] R. Muller-Fiedler, K. Jung, and H. Ehrhardt, J. Phys. B **19**, 1211 (1986).

[48] M. S. Dababneh, W. E. Kauppila, J. P. Downing, F. Lapperriere, V. Pol, J. H. Smart, and T. S. Stein, Phys. Rev. A **22**, 1872 (1980).

[49] M. S. Dababneh, Y.-F. Hsieh, W. E. Kauppila, V. Pol, and T. S. Stein, Phys. Rev. A **26**, 1252 (1982).

[50] K. P. Subramanian and V. Kumar, J. Phys. B **20**, 5505 (1987).

[51] J. C. Nickel, K. Imre, D. F. Register, and S. Trajmar, J. Phys. B **18**, 125 (1985).

[52] H. R. Skullerud, J. Phys. D **1**, 1567 (1968).

[53] S. L. Lin and J. N. Bardsley, Comput. Phys. Commun. **15**, 161 (1978).

[54] M. J. Brennan, IEEE Trans. Plasma Sci. **19**, 256 (1991).

[55] T. A. Carlson, W. E. Hunt, and M. O. Krause, Phys. Rev. **151**, 41 (1966).

[56] T. Mukoyama, T. Tonuma, A. Yagishita, H. Shibata, T. Koizumi, T. Matsuo, K. Shima, and H. Tawara, J. Phys. B **20**, 4453 (1987).

[57] H. Tawara, T. Hayaishi, T. Koizumi, T. Matsuo, K. Shima, T. Tonuma, and A. Yagishita, J. Phys. B **25**, 1467 (1992).

[58] T. Tonuma, A. Yagishita, H. Shibata, T. Koizumi, T. Matsuo, K. Shima, T. Mukoyama, and H. Tawara, J. Phys. B **20**, L31 (1987).

[59] F. Pleasonton and A. H. Snell, Proc. R. Soc. London Ser. A **241**, 141 (1957).

[60] V. Yu Chepel, Prib. Tekh. Eksp. **3**, 25 (1990) [Instrum. Exp. Tech. **33**, 497 (1990)].

[61] T. Z. Kowalski, A. Smith, and A. Peacock, Nucl. Instrum. Methods A **279**, 567 (1989).

[62] A. Peacock, B. G. Taylor, N. White, T. Courvoisier, and G. Manzo, IEEE Trans. Nucl. Sci. **32**, 108 (1985).

[63] P. Lamb, G. Manzo, S. Re, G. Boella, G. Villa, R. Andresen, M. R. Sims, and G. F. Clark, Astrophys. Space Sci. **136**, 369 (1987).

[64] J. M. F. Dos Santos, C. A. N. Conde, and A. C. S. S. M. Bento, Nucl. Instrum. Methods A **324**, 611 (1993).

[65] A. Pansky, A. Breskin, R. Chechick, and G. Malamud, Nucl. Instrum. Methods A **330**, 150 (1993).

[66] H. Inoue, K. Koyama, M. Matsuoka, T. Ohashi, and Y.

Tanaka, Nucl. Instrum. Methods **157**, 295 (1978).
[67] T. T. Hamilton, C. J. Hailey, W. H.-M. Ku, and R. Novick, IEEE Trans. Nucl. Sci. **NS-27**, 190 (1980).
[68] D. S. Simons, Ph.D. thesis, Leiden University, Holland, 1988.
[69] D. G. Simons and P. A. J. de Korte, Nucl. Instrum. Methods A **277**, 642 (1989).
[70] J. C. Bowe, Phys. Rev. **117**, 1411 (1960).
[71] J. L. Pack, R. E. Voshall, and A. V. Phelps, Phys. Rev. **127**, 2084 (1962).
[72] J. Dutton, J. Phys. Chem. Ref. Data **4**, (1975).
[73] S. S. S. Huang and G. R. Freeman, J. Chem. Phys. **68**, 1335 (1978).
[74] D. E. Cumpstey and D. G. Vass, Nucl. Instrum. Methods **171**, 473 (1980).
[75] H. L. Brooks, M. C. Cornell, J. Fletcher, I. M. Littlewood, and K. J. Nygaard, J. Phys. D **15**, L51 (1982).
[76] S. R. Hunter, J. G. Carter, and L. G. Christophorou, Phys. Rev. A **38**, 5539 (1988).
[77] T. Hashimoto and Y. Nakamura (unpublished).
[78] J. J. Lowke and J. H. Parker, Jr., Phys. Rev. **181**, 302 (1969).
[79] T. Koizumi, E. Shirakawa, and I. Ogawa, J. Phys. B **19**, 2331 (1986).
[80] M. Suzuki and S. Kubota, Nucl. Instrum. Methods **164**, 197 (1979).
[81] C. A. N. Conde, L. Requicha-Ferreira, and M. F. Ferreira, IEEE Trans. Nucl. Sci. **NS-24**, 221 (1977).
[82] F. Favata, A. Smith, M. Bavdaz, and T. Z. Kowalski, Nucl. Instrum. Methods A **294**, 595 (1990).
[83] M. Hayashi, J. Phys. D Appl. Phys. **15**, 1411 (1982).